Full-Cell Presodiation Strategy to Enable High-Performance Na-Ion Batteries

Zhen Wang, Shiming Chen, Jimin Qiu, Jiangxiao Li, Wenguang Zhao, Yuchen Ji, Xiangming Yao, Ziwei Chen, Ke Li, Mingjie Dong, Feng Pan,* and Luyi Yang*

As promising alternatives to lithium-ion batteries, sodium-ion batteries suffer from low coulombic efficiency, which stems from Na-deficiency and unstable interfaces for both cathode and anode materials. Exhibiting a favorable solvation structure, Na-naphthalene/tetrahydropyran (Na-NP/THP) is screened and selected as a full-cell presodiation solution for hard carbon (HC) anodes and a P-2 type $Na_{0.67}Fe_{0.1}Al_{0.1}Mn_{0.8}O_2$ (NFAM) cathode, which are both Na-deficient. Through a wealth of characterizations, it is revealed that the proposed presodiation agent not only boosts the initial coulombic efficiency of both HC and NFAM electrodes effectively, but also facilitates robust solid-electrolyte interphase (SEI) and cathode-electrolyte interphase (CEI) on both electrodes. Consequently, the long-term cycling and rate performance are greatly improved thanks to the stabilized structures of electrode materials. Furthermore, a proof-of-concept NFAM||HC pouch cell based on this presodiation strategy is assembled, showing a high reversible capacity and superior cycling performance. By offering a remedy to a full cell system subjected to severe Na-deficiency, this work conceptually demonstrates a feasible strategy to fully tap the potential of high-energy-density materials in sodium-ion batteries.

1. Introduction

The unprecedented demand for lithium resources has driven the cost of commercial lithium-ion batteries (LIBs) to a historic high and thus triggered the commercialization of sodium-ion batteries (SIBs). [1-3] To enable the ever-growing demands of higher energy density and long cycle life for commercial SIBs, various desirable electrode materials have been investigated in recent years. [4] However, the low initial sodium content in many reported layered oxide cathodes and the low initial Coulombic efficiency (ICE) of

Z. Wang, S. Chen, J. Qiu, W. Zhao, Y. Ji, X. Yao, Z. Chen, K. Li, M. Dong, F. Pan, L. Yang
School of Advanced Materials
Peking University Shenzhen Graduate School
Shenzhen 518055, P. R. China
E-mail: panfeng@pkusz.edu.cn; yangly@pkusz.edu.cn
J. Li
National Synchrotron Radiation Laboratory

University of Science and Technology of China Hefei 230029, P. R. China

The ORCID identification number(s) for the author(s) of this article can be found under https://doi.org/10.1002/aenm.202302514

DOI: 10.1002/aenm.202302514

hard carbon (HC) anodes result in disastrous capacity contribution in full cells.^[5–7] In order to maximize the energy density of full cells, the key is to compensate for the Na deficiency or the irreversible Na loss side reactions in either cathode or anode side.

Inspired by the prelithiation of LIBs, various presodiation methods have been successfully exploited to significantly improve the ICE of anodes and the energy density of full cells^[8–10] including direct-contact presodiation,^[11,12] half-cell presodiation,^[13,14] sacrificial additive presodiation,^[15–18] and solution presodiation.^[19–22] Among these measures, solution presodiation could achieve a mild and controllable presodiation, more importantly, it is more easily compatible with current industrial battery manufacturing processes.^[23,24]

Sun et al.^[20] firstly reported that sodium naphthaline/tetrahydrofuran (Na-NP/THF) electronic solution is used to presodiated HC anode, achieving an

increase in ICE from 67 to 87% and increasing the energy density of the full battery to 99 Wh Kg⁻¹. Subsequently, Qian et al.[22] increased the ICE of HC to 100% within 60 s by employing sodium biphenyl/dimethoxyethane (Na-BP/DME) presodiation agent. Furthermore, the analogous approaches had been applied to the presodiation of reduced graphene oxide, [25] antimony, [21] tin, [26] and phosphorus anodes, [19,26] which has achieved significant effects in the improvement of ICE and energy density. Nevertheless, when a Na-deficient (e.g., P-2 type) cathode is coupled with HC anode, a large excess amount of active Na required. It should be noted that loading all these extra Na on the anode would inevitably result in a significant decrease in the air-stability of the anode, which is unfavorable for battery assembling and long-term storage. [27] On the other hand, it also requires to avoid damaging the structure of cathode during the presodiation process. Therefore, a universal full-cell presodiation strategy for this seemly "bad match" is highly desirable which helps to promote the development of high-energy-density SIBs.

Herein, through theoretically and experimentally screening various solutions, a solution based on naphthalene (NP) and tetrahydropyran (THP) is proposed as a safe and facile presodiation agent for both Na-deficient P-2 cathode (Na $_{0.67}$ Fe $_{0.1}$ Al $_{0.1}$ Mn $_{0.8}$ O $_{2}$, denoted as NFAM) and sodium-free

16146840, 2023, 45, Downloaded from https://advancec

onlinelibrary.wiley.com/doi/10.1002/aenm.202302514 by University Town Of Shenzhen, Wiley Online Library on [20/11/2025]. See the Terms

onditions) on Wiley Online Library for rules of use; OA articles are governed by the applicable Creative Commons

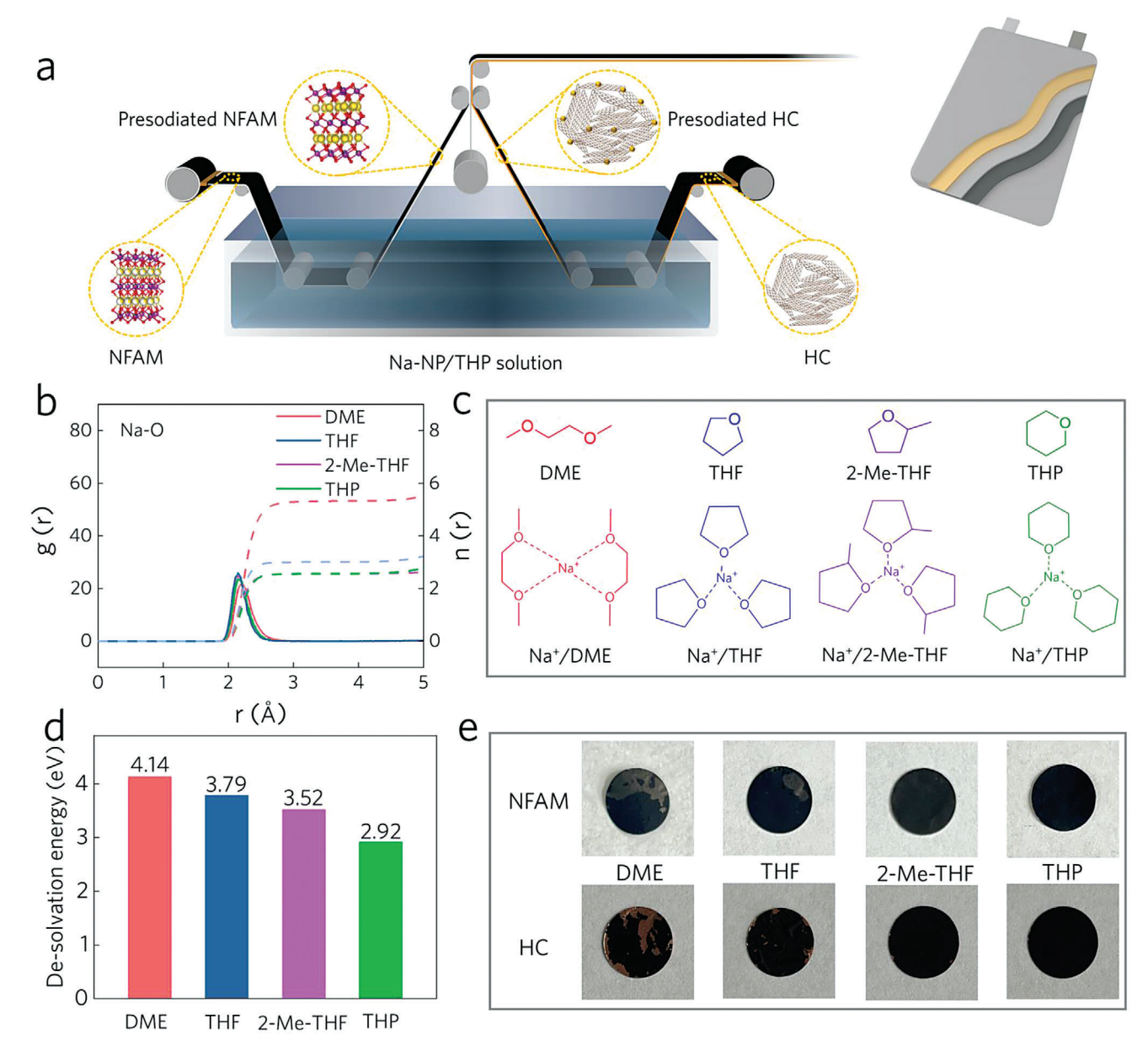


Figure 1. a) Schematic illustration of the solution presodiation method for commercial roll-to-roll cell manufacturing process. b) Calculated radial distribution functions (g(r), solid line) and corresponding coordination numbers (n(r), dash line) for DME, THF, 2-Me-THF, THP. c) Molecular structures of potential solvents (DME, THF, 2-Me-THF, THP) and the corresponding solvated structures with Na⁺. d) Comparison of de-solvation energy barrier of Na⁺-solvent (DME, THF, 2-Me-THF, THP) complexes. e) Optical photographs of both electrodes after pretreatment in different presodiation solutions.

HC anode simultaneously, which could be readily implemented into the commercial roll-to-roll process (**Figure 1a**). After presodiation, the ICE of both HC and NFAM can be greatly promoted. More importantly, it is revealed that the proposed presodiation strategy constructs robust interphases on both electrodes, which not only mitigate undesirable interfacial side reactions (e.g., solid-electrolyte interphase/cathode-electrolyte interphase (SEI/CEI) dissolution and transition metal dissolution) but also expedites interfacial charge transfer on both electrodes. Consequently, improved rate performance and cycle stability can be obtained in both half and full cells.

2. Result and Discussion

2.1. Screening of Solvents

The redox potential of a presodiation agent is closely related to the electron affinity of the solute and solvent molecules: lower electron affinity generally results in lower redox potential of the corresponding presodiation agent, hence the greater presodiation capability. [28,29] It is worth noting that, in addition to the redox potential, the solvated structures formed by Na⁺ and solvent molecules are also crucial for presodiation. Due to the different

ADVANCED ENERGY MATERIALS 16146480, 2023, 45, Dwnholaded from https://dwnneed.onlinelibrary.wiely.com/oi/010.002/aen.20.202514 by University Town Of Sheraben, Wiley Online Library on [2011.1025]. See the Terms and Conditions (https://onlinelibrary.wiely.com/terms-and-conditions) on Wiley Online Library for rules of use; OA articles are governed by the applicable Cerative Commons

solvation energy, solvent molecules and charge carriers (i.e., Na⁺) generally form four types of solvated structures, including contact ion pairs (CIPs), aggregated ion pairs (AIPs), solvated ions (SIs) and solvent-separated ion pairs (SSIPs).^[30] Among these configurations, SIs and SSIPs favor the co-intercalation of solvent molecules, thus causing damage to the structure of electrode materials. The solvation structures of presodiation reagents depend on the desolvation energy and the molecular configuration of solvent molecule: solvents exhibiting high desolvation energy and small steric hindrance tend to form SIs or SSIPs, causing solvent co-intercalation.^[28,30] In order to achieve presodiation without damaging the structure of electrode materials, in this work, different presodiation agents were screened according to their redox potential, desolvation energy, and molecular configuration.

Owing to the nature of strong electronegativity, BP and NP can easily take electrons from sodium to form Na-arene complex, thus they are widely used as solutes in chemically presodiated solutions. [20,22,25,26] However, the lower reduction potential of BP compared with NP results in a more violent presodiation, making it more difficult to control the degree of presodiation.^[20,25,29] Therefore, we chose NP as a milder solute for the preparation of presodiation solution. In addition to solute, the choice of solvent is also important for the effectiveness of solution presodiation. Therefore, in this work, DME, THF, 2-Methyl-tetrahydrofuran (2-Me-THF), and THP are screened as four potential candidates. Based on the analysis results of calculated radial distribution function (Figure 1b; Figure S1, Supporting Information), the representative solvation structures of Na-NP formed in four different solvents are obtained (Figure 1c). Compared with the other three solvents, DME possesses significantly more coordinated oxygen atoms with Na⁺, suggesting a relatively robust solvation structure with Na+ (Figure S2, Supporting Information). Furthermore, the similar conclusion is obtained from density functional theory calculations (Figure 1d). Among these four solvents, DME possesses the highest de-solvation energy barrier (4.14 eV), indicating that Na⁺ tends to coordinate with DME to form SIs or SSIPs, which could lead to co-intercalation of solvent molecules and consequently the structural degradation of electrode materials.^[28] In comparison, THP possesses the lowest de-solvation energy barrier (2.92 eV), indicating that Na+ tends to form CIPs or AIPs in Na-NP/THP solution. THP also has a larger solvated molecular volume compared to other solvents (Figure S3, Supporting Information), which implies that the solvated structure displays a large steric hindrance, [31,32] inhibiting the solvent co-intercalation. Therefore, the embedding of naked Na⁺ is preferred in THP, which is beneficial to maintain the structural stability of electrode materials. To verify the above speculation, electrodes were immersed in different solutions for presodiation. As expected (Figure 1e), solvents with higher de-solvation energy barrier result in disintegration of both electrodes, suggesting large variation of particle size caused by solvent co-intercalation. The cycling stability of electrodes pretreated by different solvents also verifies the conclusion, where THP outperforms other solvents (Figure S4, Supporting Information). Based on the above analysis, Na-NP/THP was finally chosen solution as the presodiation reagent as it was benign to both electrodes while other agents exhibited detrimental effects.

2.2. Presodiation of Hard Carbon (HC) Anode

As shown in **Figure 2**a and Figure S5 (Supporting Information). the ICE of HC can be improved from 61% to almost unity after immersed in Na-NP/THP, demonstrating that the presodiation treatment eliminates the initial irreversible capacity. From the cyclic voltammetry (CV) profiles of HC anode, the reduction peak (≈0.9 V) corresponding to SEI formation disappeared after presodiation, suggesting that an SEI film has already been formed on the surface of HC anode (Figure S6, Supporting Information). To test the air-stability of presodiated HC, anodes with ICEs of 87%, 99%, and 107% (denoted as HC-87, HC-99, and HC-107, corresponding to incompletely presodiated, fully presodiated, and excessively presodiated HC, respectively) were rested in dry air for 24 h (Figure 2b). As expected, the excessively presodiated HC (HC-107) suffer from severe dive in ICE and sharp increase in open circuit voltage (OCV), owing to its high reactivity towards moisture and oxygen. By contrast, with only slightly compromised ICEs and OCVs, both HC-87 and HC-99 anodes exhibit satisfactory air-stability. Based on this result, it is reasonable to speculate that the ICE value of HC should not exceed 100% for the sake of electrode storage. Therefore, the fully presodiated HC-99 will be adopted in the rest of this study. Results of both X-ray photoelectron spectroscopy (XPS) characterization (Figure S7, Supporting Information) and energy dispersive X-ray spectroscopy (Figure S8, Supporting Information) confirm Na embedding.

Various mechanisms have been reported regarding to Na storage in HC anode, including adsorption, intercalation, and pore filling.[33] To investigate where the presodiation embedded Na⁺ are stored, in situ Raman characterization was conducted. Figure 2c exhibits that the discharge process of the pristine HC can be divided into two stages: first (Stage I), the Gband is almost unchanged and the D-band gradually weakens; subsequently (Stage II), the G-band gradually shifts toward a lower wave number, showing that Na storage in HC follows an adsorption-insertion mechanism.[34] For the presodiated HC (Figure 2d), only the G-band excursion occurs during the first discharge, indicating that the Na+ introduced by the presodiation process are adsorbed on the surface, defect, vacancy, or edge of HC. The initial charge/discharge curves of presodiated HC (Figure S9, Supporting Information) show significantly lower adsorption capacity, implying that the presodiation process loads Na⁺ to the irreversible adsorption sites of HC.^[35] Furthermore, the (002) crystal plane in presodiated HC has no shift, which supports the above speculation (Figure S10, Supporting Information). When charged to 2.0 V, both G-bands and D-bands shift back, suggesting that the Na⁺ extraction/insertion processes in both HC anodes are reversible and the presodiation does not affect the structure of the HC.

Next, the rate performance and cycling stability of presodiated and pristine HC are compared in **Figure 3**a,b, respectively. Under the specific current of 800 mA g^{-1} , the presodiated HC could release a much higher capacity (246 mAh g^{-1}) compared with the pristine one (199 mAh g^{-1}). The superior rate capability of presodiated HC can be attributed to the lowered interfacial impedance after presodiation (Figure S11, Supporting Information). The long-term cycling stability of HC was tested under different specific currents. Under 200 mA g^{-1} the capacity

16146840, 2023, 45, Downloaded from https://advanced.onlinelibrary.viley.com/ab/10.1002/aemm. 202302514 by University Town Of Shenzhen, Wiley Online Library on [20112025]. See the Terms and Conditions (https://onlinelibrary.wiely.com/terms/

and-conditions) on Wiley Online Library for rules of use; OA articles are governed by the applicable Creative Commons

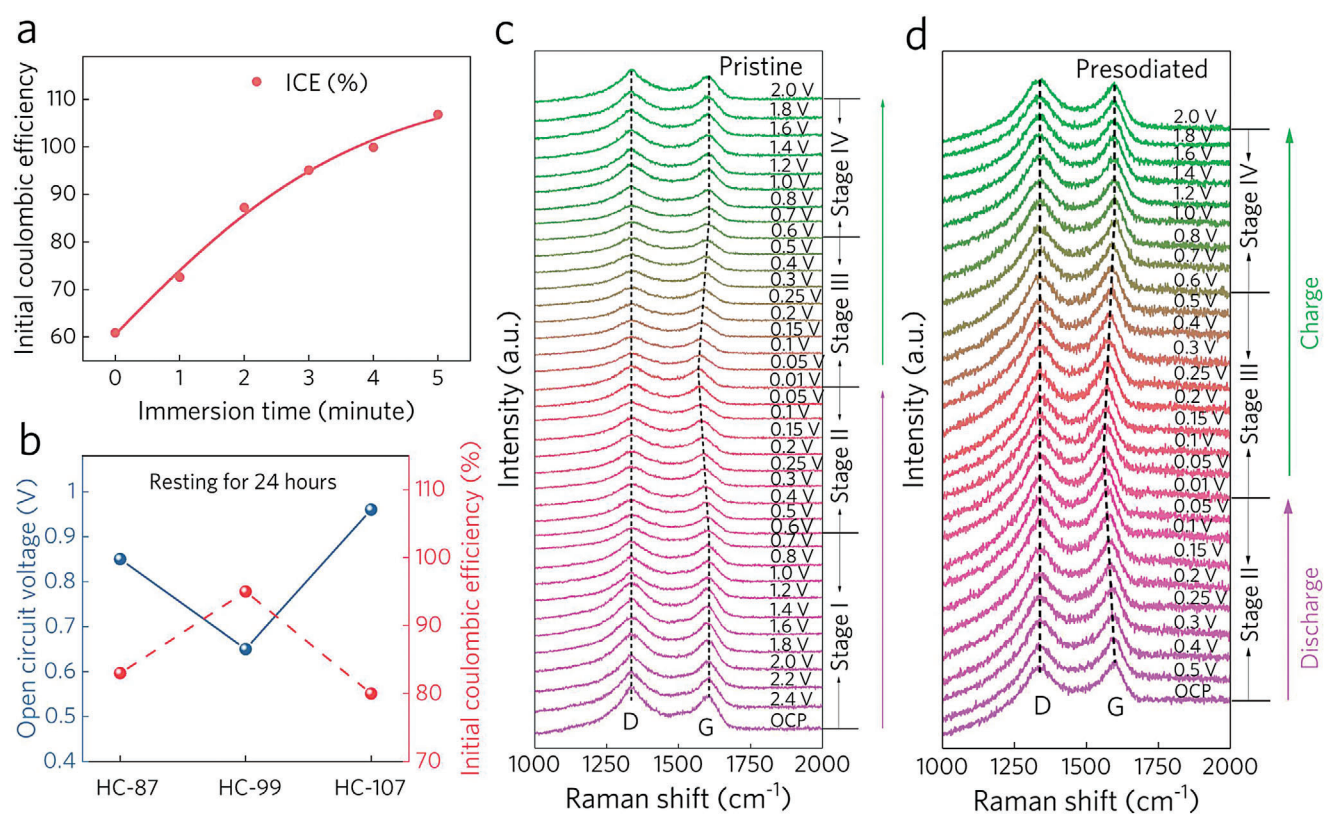


Figure 2. a) Relationship between ICE and presodiation time for HC anode. b) Comparison of ICE and OCV of presodiated HC with various degrees of presodiation before and after 24 h of resting in dry air with a dew point temperature of -45 °C. In situ Raman spectroscopy of the c) pristine and d) presodiated HC anode.

retention of the presodiated HC was 79.3% after 1000 cycles, while the pristine HC only exhibited a retention of 45.6%. Similar results can be obtained under 50 mA g^{-1} (Figure S12, Supporting Information). Also, the same results were observed for an alternative HC anode, which further proves the universality of this strategy (Figure S13, Supporting Information). The improved cycling stability of presodiated HC is also reflected in full-cell performance when coupled with commercial Na-rich Na₃V₂(PO₄)₃ cathode (Figure S14, Supporting Information).

To investigate the underlying mechanisms for the enhanced electrochemical performance, the morphological information of HC was first examined. As shown in Figure S15 (Supporting Information), the open pores inside HC disappeared after presodiation. Since these pores contribute a large portion of irreversible side reactions, [36] this difference in bulk morphology accounts for the improved ICE. Furthermore, the scanning electron microscopy (SEM) images shows that the surface of the presodiated HC particles has become much smoother without pores compared with pristine HC (Figure S16, Supporting Information). According to the cryo-transmission electron microscopy (cryo-TEM) images (Figure 3c; Figure S17, Supporting Information), a uniform SEI layer can be found on the presodiated HC surface. In order to investigate the composition of the SEI layer, XPS characterization was performed before cycling (Figure S7, Supporting Information). The C-F peak in the pristine HC electrode, which corresponds to poly(vinyl difluoride) (PVDF) binder, cannot be detected in the presodiated HC electrode, as it might be masked

by the SEI induced by presodiation. Instead, a strong peak of NaF can be found on the presodiated HC electrode, which coincides with the lattice fringe of NaF observed in the cryo-TEM result above. XPS, Raman, and Fourier Transform infrared spectroscopy results of PVDF polymer films treated with Na-NP/THP solution (Figure S18, Supporting Information) confirm that NaF originates from the chemical reaction between the presodiated solution and PVDF. Similar to LiF,^[37] NaF is considered as a favorable component in the SEI owing to its desirable ionic conductivity, chemical stability, and high mechanical strength,^[38,39] which not only effectively alleviate electrolyte decomposition, but also improves the interfacial transfer kinetics of Na⁺. Hence, the presodiated HC exhibits superior rate performance and cycling stability.

Electrochemical quartz crystal microbalance (EQCM) was employed to test the stability of this SEI layer^[40] (Figure 3d,e), where both HC electrodes were scanned to 0.01 V versus Na/Na⁺ and rested for a period. Both pristine and presodiated HC display continuous increase of mass during scanning, which is related to Na⁺ insertion and SEI formation. During the resting process, the mass of the pristine HC anode starts to decrease, which could be attributed to the dissolution of electrochemically formed SEI.^[41,42] In sharp contrast, the mass of the pretreated HC remains almost constant. This difference might be resulted from the higher total content of organic species (C—O, C=O, and—CO₃) on the pristine HC than that of pretreated HC (Figure 3f), which are more soluble in the electrolyte. For the presodiated HC,

16146840, 2023, 45, Downloaded from https://advanced.onlinelibrary.wiky.com/doi/10.1002/semm.202302514 by University Town Of Shenzhen, Wiley Online Library on [2011/2025]. See the Terms and Conditions (https://onlinelibrary.wiky.com/term/

and-conditions) on Wiley Online Library for rules of use; OA articles are governed by the applicable Creative Commons

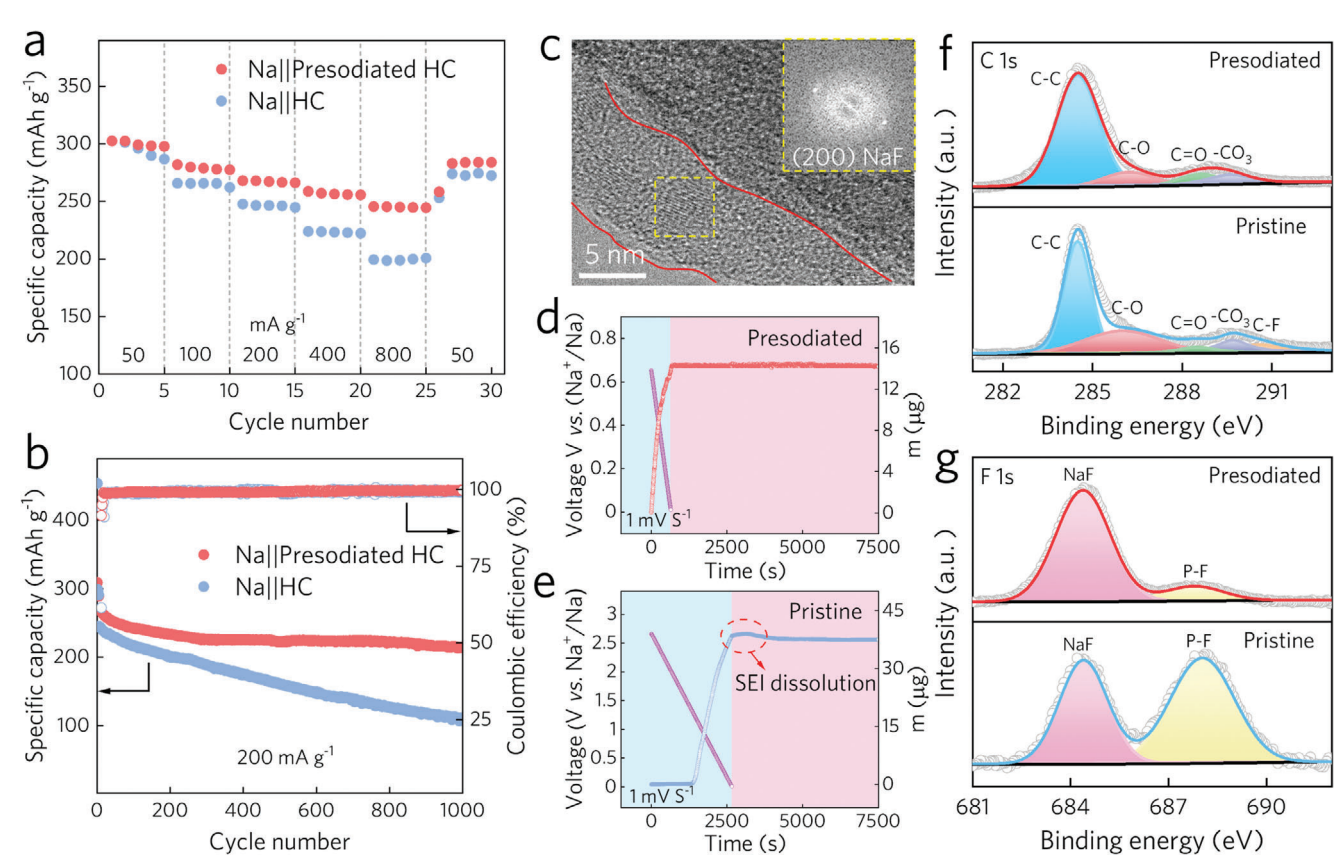


Figure 3. a) Galvanostatic rate testing and b) cycling performance of HC anode before and after presodiation. c) Cryo-TEM image of the presodiated HC anode. EQCM tests of d) presodiated and e) pristine HC anodes during a cathodic scanning rate of 1 mV s⁻¹ (blue region) and resting period (red region). f) C 1s and F 1s (g) XPS spectra of the presodiated and pristine HC anode after cycling.

the much stronger peak of NaF compared with P-F also shows that NaF is a dominant composition in the SEI (Figure 3g).

2.3. Presodiation for Na_{0.67}Fe_{0.1}Al_{0.1}Mn_{0.8}O₂ (NFAM) Cathode

Similar to the results of HC anode, the presodiated NFAM also shows much-improved ICE (Figure S19, Supporting Information) due to the insertion of additional Na⁺ (Table S1, Supporting Information). According to the electrochemical curves and results of inductively coupled plasma emission spectrometry, pprox 0.2 active Na (pprox 50 mAh g $^{-1}$) was introduced to materials to achieve an ICE ≈100%. And Mn L-edge soft X-ray absorption spectroscopy (sXAS) results (Figure 4a) exhibit a significant decrease of Mn3+ on surface of the presodiated NFAM compared with pristine NFAM, suggesting the reduction of Mn3+ due to the chemical insertion of Na⁺. Also, part of Mn³⁺ is reduced to Mn²⁺ in bulk phase that is confirmed by Mn L-edge sXAS total fluorescence yield spectra and in-depth XPS spectra (Figure S20, Supporting Information). In addition, valence states of Fe and Al have barely changed during the presodiation process (Figure S21, Supporting Information). The repetitive CV curves of different cycles indicate that the redox reactions of Mn²⁺/Mn³⁺ are highly reversible during the electrochemical process (Figure S22, Supporting Information). Furthermore, the presodiated NFAM exhibits superior rate capability (Figure S23, Supporting Information) and capacity retention (Figure 4b) compared with the pristine NFAM. Similarly, this strategy is shown to be effective for an alternative P-2 type cathode (Na_{0.67}Fe_{0.2}Mn_{0.8}O₂) with higher specific capacities (≈150 mAh g⁻¹), demonstrating its potential in realizing high-energy-density SIBs (Figure S24, Supporting Information). As shown in Figure S25, Supporting Information, D_{N2+} of presodiated NFAM exhibits higher values than the pristine cathode during the cycle, which can be attributed to the lager interlayer spacing. To probe into the correlation between the superior electrochemical properties and the structural stability of NFAM after presodiation, a series of characterizations have been performed. X-ray diffraction (XRD) patterns of the prosodiated NFAM exhibit a slight shift of (002) peak to a high angle, which is a typical feature for the insertion of Na⁺ into cathode lattice (Figure S26, Supporting Information). In situ XRD was also performed to monitor the structure evolution process of both cathodes during the first two cycles (Figure 4c,d). In order to quantify the structural variation, the corresponding lattice parameters were obtained from Rietveld refinements.^[43] Evidently, the (002) peaks of both cathodes gradually shift to a lower angle during the charging process, corresponding to the extended *c*-axis, which is induced by the increased electrostatic repulsion between adjacent TMO₂ slabs with Na⁺ extraction. Additionally, owing to the oxidization of transition metal ions, the (100) and (102) peaks of both cathodes shift to higher angles, corresponding to contractive aaxis (Figure S27, Supporting Information). The reverse change in

16146840, 2023, 45, Downloaded from https://advanced.onlinelibrary.wiley.com/doi/10.1002/nemm.202302514 by University Town Of Shenzhen, Wiley Online Library on [20/11/2025]. See the Terms

on Wiley Online Library for rules of use; OA articles are governed by the applicable Creative Commons

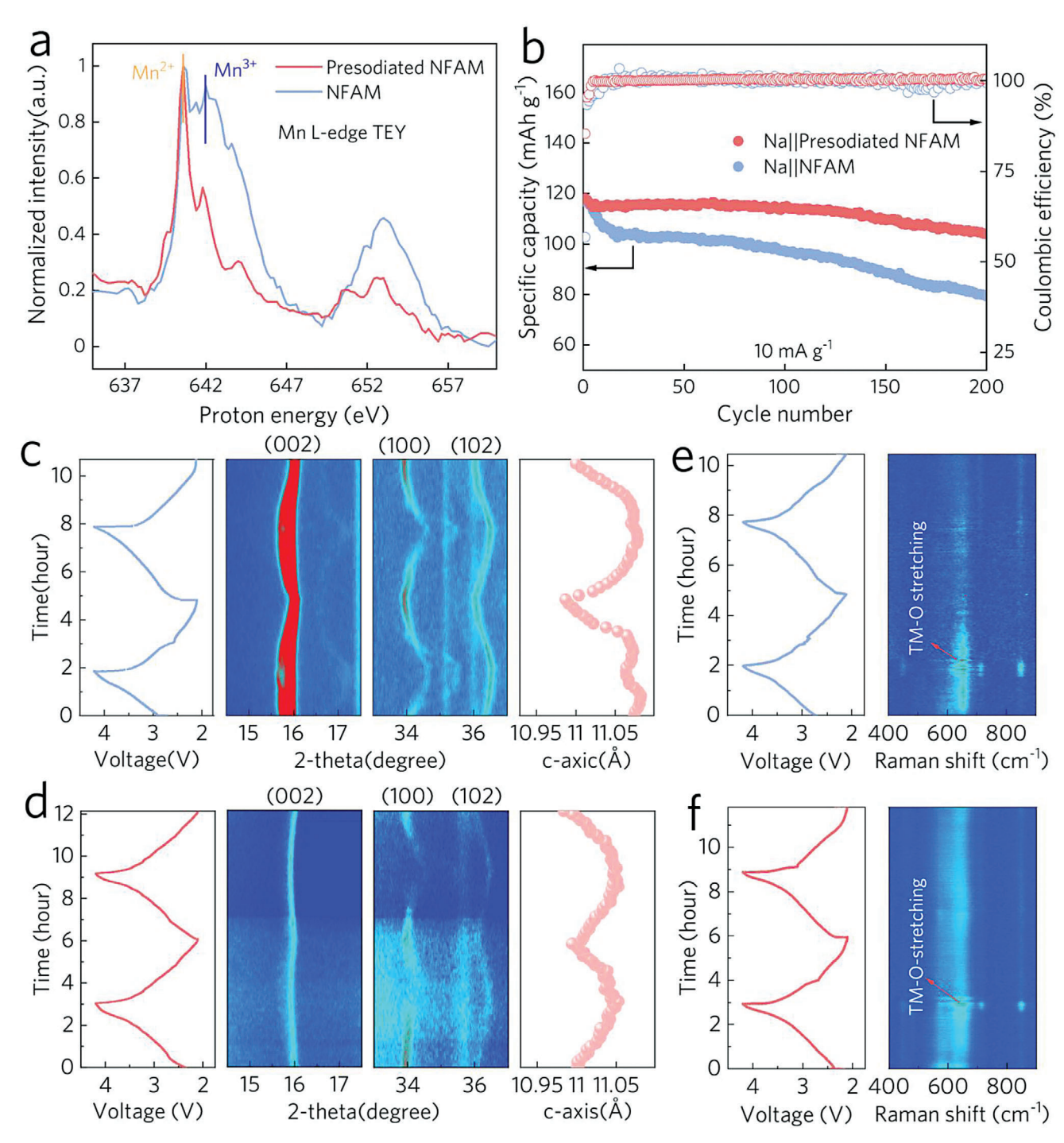


Figure 4. a) Manganese L-edge sXAS results of NFAM cathode before and after presodiation in total electron yield mode. b) Galvanostatic cycling performance of NFAM cathode before and after presodiation. In situ XRD patterns and the corresponding c-axis lattice parameter changes obtained from Rietveld refinements during the first two cycles of the c) pristine and d) presodiated NFAM cathode at 30 mA g⁻¹ between 2.1 and 4.2 V. In situ Raman spectroscopy of the e) pristine and f) presodiated NFAM cathode at 30 mA g⁻¹ between 2.1 and 4.2 V.

lattice parameters can be clearly observed during discharge processes. It is noteworthy that the c-axis of the Na-deficient cathode contracted slightly when charged above 3.6 V, which can be attributed to the interlayer dislocation at deep charging state. In contrast, the Na-rich cathode exhibited smaller expansions of

c-axis at high voltage region, without obvious abnormal c-axis contraction. Consequently, it is rational to speculate that the Narich cathode can maintain more Na⁺ in Na slab at high voltage, which weakens the electrostatic repulsion to suppress c-axis expansion and prevent interlayer slips. The inhibition of interlayer

16146840, 2023, 45, Downloaded from https://advanced.onlinelibrary.wiley.com/doi/10.1002/aemm.202302514 by University Town Of Shenzhen, Wiley Online Library on [2011/2025]. See the Terms and Conditions (https://onlinelibrary.wiley.com/terms

and-conditions) on Wiley Online Library for rules of use; OA articles are governed by the applicable Creative Commons

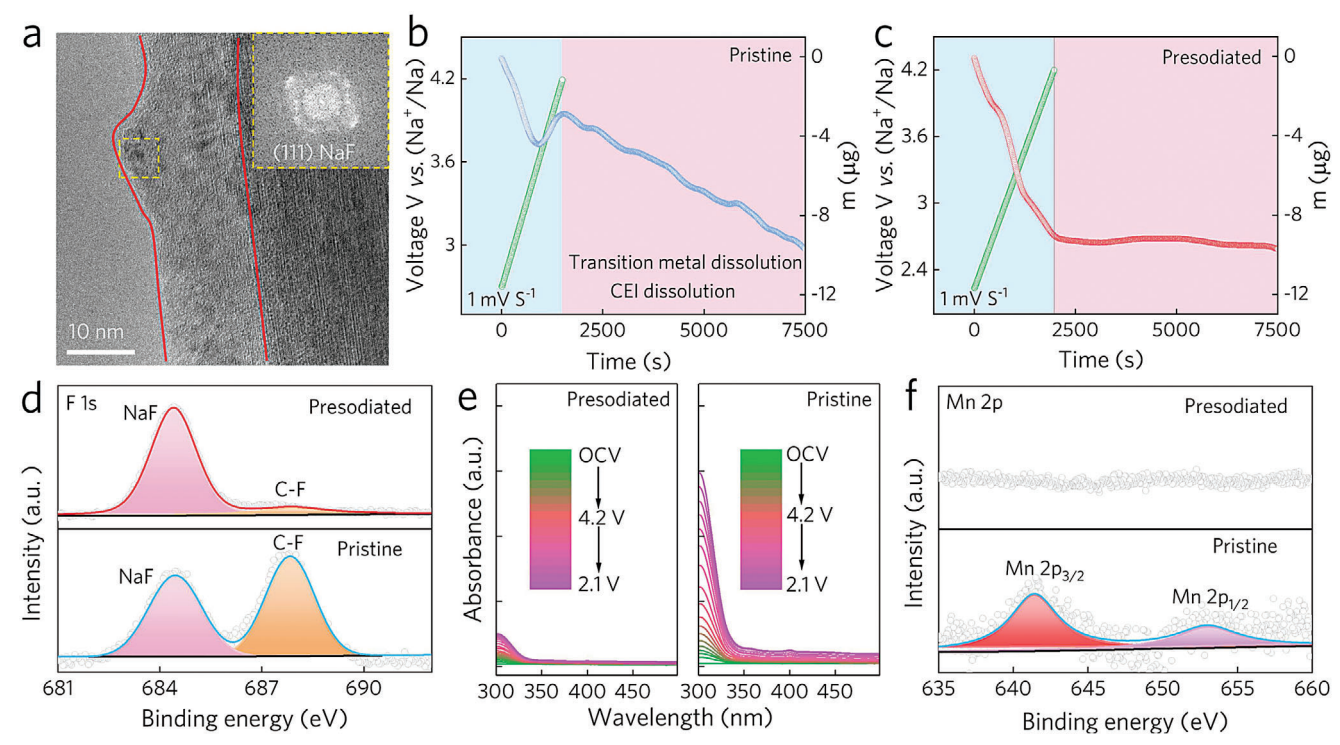


Figure 5. a) Cryo-TEM image of the presodiated NFAM cathode. EQCM tests of b) pristine and c) presodiated NFAM cathode at a scanning rate of 1 mV s⁻¹. d) F 1s spectra of NFAM cathode with/without presodiation after cycling. e) In situ UV–vis spectra of the presodiated and pristine NFAM cathode. f) Mn 2p spectra of sodium metal disc with/without presodiation after cycling.

spacing variation and slab slips in Na-rich cathode efficiently improves the structural stability during repeated Na⁺ intercalation and de-intercalation.

The investigations of near-surface structure evolutions were conducted by in situ Raman spectroscopy. As shown in Figure 4e,f, the Raman peaks observed at ≈650 cm⁻¹ can be attributed to TM-O stretching in layered sodium ion battery cathodes.[44] For Na-deficient cathode, the Raman signals at ≈650 cm⁻¹ faded away during the initial two cycles, indicating the collapse of the layered structure on the near-surface region. In sharp contrast, the Na-rich cathode can remain well layered structure at the surface since the corresponding Raman peak remain stable. In addition, after charged above ~ 4.0 V at the initial cycle, the new Raman peaks observed at ≈720 and ≈850 cm⁻¹ in both cathodes can be attributed to the formation of oxidized electrolyte species on the surface of cathodes. [45] The presodiated NFAM exhibits much weaker interfacial decomposition peaks compared with the pristine NFAM, suggesting a more stable interfacial structure during long-term cycling.

Similar to HC anode, the SEM results show that the surface of the NFAM after presodiation is much smoother compared to the pristine NFAM (Figure S28, Supporting Information), which is due to the formation of a dense and uniform cathode electrolyte interface (CEI, **Figure 5**a; Figure S29, Supporting Information). With emerging peaks of $-CO_3$ and NaF, the C1s and F1s XPS spectra of presodiated NFAM are very similar to those of presodiated HC (Figures S7 and S30, Supporting Information), suggesting the chemical compositions of preformed CEI/SEI on NFAM/HC mainly depend on sodiation agents and binders.

This finding further increases the feasibility of this work in full cells since a symmetric "CEI-SEI" is reported to be beneficial for matching interfacial charge transfer kinetics and capacity between anodes and cathodes. [46]

Considering such CEI is formed under reductive environment, it is necessary to examine its stability against oxidation. EQCM results (Figure 5b) show that during positive scanning, the electrode mass of pristine NFAM first decreased due to the deintercalation of Na+; upon 3.6 V, the mass started to increase due to the formation of a large amount of CEI, which outweighed the Na+ deintercalation process. For the presodiated NFAM (Figure 5c), the mass variation trend remained negative, suggesting the preformed CEI has effectively passivated the electrode, hence the electrochemically formed CEI is negligible. During the resting period, a dramatic mass decrease can be recorded for the pristine NFAM, which originates from the dissolution of CEI and transition metal. By contrast, the mass of the presodiated NFAM barely changed with time, which indicates that the preformed CEI is more robust than the CEI formed by cycling process. This conclusion is further supported by the post-cycling XPS spectra (Figure 5d).

To investigate the impact of CEI on transition metal dissolution, in situ ultraviolet-visible (UV–vis) spectroscopy analysis (Figure 5e; see the set up in Figure S31, Supporting Information) was carried out. the absorption peak of transition metal intensified as charging and discharging proceed, indicating continuous transition metal dissolution; whereas the intensity and growth rate of the absorption peak for the presodiated NFAM are significantly lower than that of the pristine one. The XPS spectra of Mn

16146840, 2023, 45, Downloaded from https://advanced.onlinelibrary.wiley.com/doi/10.1002/aemm.202302514 by University Town Of Shenzhen, Wiley Online Library on [20/11/2025]. See the Terms

ınd-conditions) on Wiley Online Library for rules of use; OA articles are governed by the applicable Creative Commons

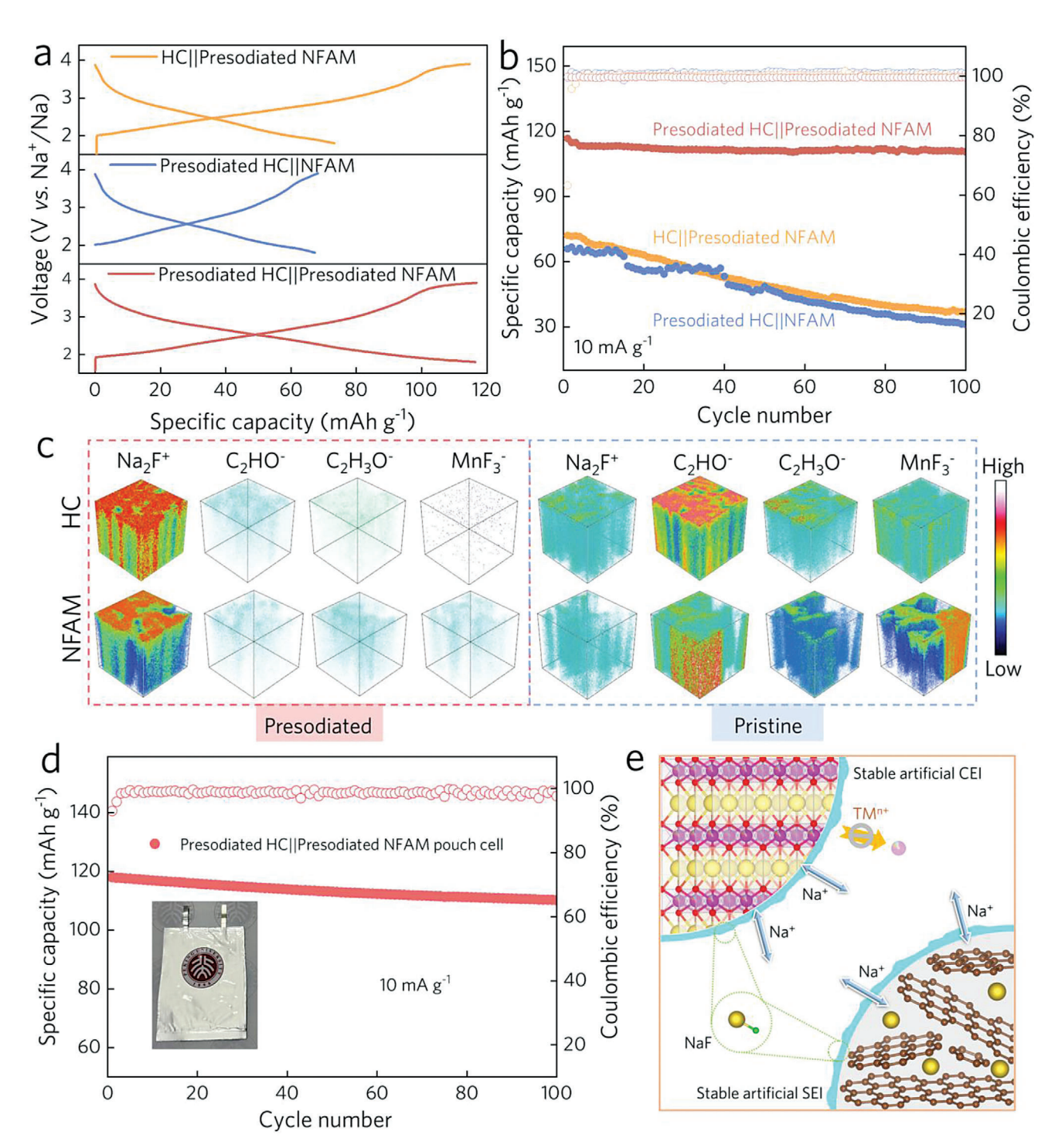
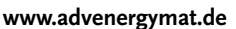


Figure 6. a) Initial charge-discharge curves and b) the corresponding cycling performance of different HC||NFAM full cells at a current density of 10 mA g^{-1} . c) TOF-SIMS 3D distribution maps of several representative secondary ion fragments obtained from the electrodes of presodiated and pristine full cells after cycling. d) Cycling performance of presodiated HC||presodiated NFAM pouch cell. e) Schematic illustration of the effect of the presodiation method on the improved HC||NFAM full cell performance.

www.advancedsciencenews.com



ADVANCED ENERGY MATERIALS 16146840, 2023. 45, Downloaded from https://advanced.onlinelibrary.wiley.com/doi/10.1002/aemn.202302514 by University Town Of Shenzhen, Wiley Online Library on [2011/2025]. See the Terms and Conditions (https://onlinelibrary.wiley.com/terms

and-conditions) on Wiley Online Library for rules of use; OA articles are governed by the applicable Creative Commons

2p from the post-cycling sodium disc (Figure 5f) also confirmed that Mn dissolution in the presodiated NFAM is constrained, which again proves that the CEI could mitigate the dissolution of transition metal, enabling robust structure and outstanding electrochemical performance. [47,48] In summary, the proposed presodiation strategy not only improves the structural stability of bulk NFAM, but also facilitates a robust CEI to suppress unwanted side reactions.

2.4. Full Cell Performance

In order to practically verify the improvement effect of the presodiation method on both NFAM cathode and HC anode, full cells equipped with both pristine and presodiated electrodes were assembled. As shown in Figure 6a and Figure S32a (Supporting Information), when only the cathode is presodiated, although the charge capacity can reach as high as 115 mAh g⁻¹, the irreversible reaction of the HC anode consumes active Na+, resulting in a discharge capacity of only 73 mAh g⁻¹. Whereas when only the anode side is presodiated, although the initial irreversible capacity loss was eliminated, the charge capacity was too low (68 mAh g⁻¹). If both electrodes were presodiated, a high reversible capacity could be achieved 116 mAh g⁻¹ with a Coulomb efficiency close to 100%, thus significantly increasing the energy density of the full cell. Accordingly, a much-improved energy density (247 Wh kg⁻¹, calculated based on the total mass of active materials) can be obtained by presodiated HC||presodiated NFAM compared with that of HC||presodiated NFAM (156 Wh kg⁻¹), presodiated HC||NFAM (146 Wh kg⁻¹) and HC||NFAM (86 Wh kg⁻¹). Figure 6b and Figure S32b (Supporting Information) display the long-term cycling performance of the above four full-cells. For the full cell of both presodiated electrodes, it still provides a superior specific capacity of 111 mAh g⁻¹ after 100 cycles, demonstrating excellent cycling performance. However, the other two cells equipped with only one presodiated electrode show unsatisfactory cyclic stability. The discrepancy in full-cell performance could be attributed to the similar chemical composition and morphology in CEI and SEI, which effectively regulate the interfacial charge transfer kinetics in both electrodes.

Next, time-of-flight secondary-ion mass spectrometry (TOF-SIMS) test was implemented to investigate the surface information of full cells. According to 3D visual maps (Figure 6c) and the corresponding depth profiles (Figure S33, Supporting Information), both anode and cathode in the prsodiated cell exhibit strong Na₂F⁺ fragment signals on their surfaces, implying that the SEI/CEI component is dominated by inorganic NaF. Meanwhile, the fragment signals representing organic decomposition species (C2HO- and C2H3O-) and transition metal ions (MnF₃⁻) are very weak, which is attributed to the dense and robust SEI/CEI prebuilt by presodiation that effectively suppresses the undesirable side reactions during cycling. In contrast, SEI/CEI formed on pristine electrodes are composed of abundant organic component and a little NaF. In addition, the significantly intensified MnF₃⁻ fragment signal indicates drastic transition metal dissolution compared to the pretreated cell, which is a main failing cause of full cells.

To further demonstrate the feasibility of this presodiation method in scale-up manufacture, pouch cells using presodiated HC and presodiated NFAM were assembled and tested (Figure 6d). The presodiated HC||presodiated NFAM pouch cell delivered a discharge capacity as high as 116 mAh $\rm g^{-1}$ with a coulombic efficiency of 93.1% in the initial cycle, and a capacity retention of 93.4% was achieved after 100 cycles, exhibiting superior capacity retention compared with those previously reported P-2 type cathodes (Table S2, Supporting Information). As concluded in Figure 6e, the excellent electrochemical performance of full cells can be attributed to the pre-compensation of active Na in the electrodes as well as the pre-construction of robust CEI/SEI by presodiation.

3. Conclusion

Herein, through screening solvated structures, Na-NP/THP solution was employed as the presodiation agent for both HC anode and NFAM cathode. On the anode side, Na-NP/THP embeds active Na+ into HC and pre-forms a robust NaF-rich SEI on the surface of HC, which efficiency alleviates the extensive electrolyte reductive decomposition during the initial discharge process and suppresses the repeated dissolution-regeneration of unstable SEI during subsequent cycles. As for the cathode, the pre-embedded Na⁺ by presodiation reinforces the structure stability of Na-deficient NFAM cathode. In addition, the robust NaFrich CEI pre-formed on NFAM prevents undesirable oxidative decomposition of electrolyte as well as transition metal dissolution. Therefore, due to the synergistic effect of presodiation on the improvement of HC anode and NFAM cathode, the presodiated HC||presodiated NFAM full cell provides a high reversible capacity of 111 mAh g⁻¹ after 100 cycles and presodiated HC||presodiated NFAM pouch cell achieves a satisfactory capacity retention of 93.4% after 100 cycles. This work aims to provide new insights into the optimization of electrochemical performance (especially energy density) of batteries employing Na(Li)deficient or Na(Li)-free electrodes.

Supporting Information

Supporting Information is available from the Wiley Online Library or from the author.

Acknowledgements

Z.W., S.C., and J.Q. contributed equally to this work. This work was supported by the Soft Science Research Project of Guangdong Province (no.2017B030301013), the Shenzhen Science and Technology Planning Project (JSGG20220831095604008). The authors thank Shanghai Synchrotron Radiation Facility (SSRF) (beamline 02B02) for the allocation of synchrotron beam time.

Conflict of Interest

The authors declare no conflict of interest.

Data Availability Statement

Research data are not shared.

www.advancedsciencenews.com

www.advenergymat.de

ADVANCED ENERGY MATERIALS

16146840, 2023, 45, Downloaded from https://advanced.onlinelibrary.wiley.com/doi/10.1002/tenm.202302514 by University Town Of Shenzhen, Wiley Online Library on [20/11/2025]. See the Terms and Condition (https://onlinelibrary.wiley.com/doi/10.1002/tenm.202302514 by University Town Of Shenzhen, Wiley Online Library on [20/11/2025]. See the Terms and Condition (https://onlinelibrary.wiley.com/doi/10.1002/tenm.202302514 by University Town Of Shenzhen, Wiley Online Library on [20/11/2025]. See the Terms and Condition (https://onlinelibrary.wiley.com/doi/10.1002/tenm.202302514 by University Town Of Shenzhen, Wiley Online Library on [20/11/2025]. See the Terms and Condition (https://onlinelibrary.wiley.com/doi/10.1002/tenm.202302514 by University Town Of Shenzhen, Wiley Online Library on [20/11/2025]. See the Terms and Condition (https://onlinelibrary.wiley.com/doi/10.1002/tenm.202302514 by University Town Of Shenzhen, Wiley Online Library on [20/11/2025]. See the Terms and Condition (https://onlinelibrary.wiley.com/doi/10.1002/tenm.202302514 by University Town Of Shenzhen, Wiley Online Library on [20/11/2025]. See the Terms and Condition (https://onlinelibrary.wiley.com/doi/10.1002/tenm.202302514 by University Town Of Shenzhen, Wiley Online Library on [20/11/2025]. See the Terms and Condition (https://onlinelibrary.wiley.com/doi/10.1002/tenm.202302514 by University Town Of Shenzhen, Wiley Online Library on [20/11/2025]. See the Terms and Condition (https://onlinelibrary.wiley.com/doi/10.1002/tenm.202302514 by University Town Of Shenzhen, Wiley Online Library on [20/11/2025]. See the Terms and Condition (https://onlinelibrary.wiley.com/doi/10.1002/tenm.202302514 by University Town Of Shenzhen, Wiley Online Library on [20/11/2025]. See the Terms and Condition (https://onlinelibrary.wiley.com/doi/10.1002/tenm.202302514 by University Town Of Shenzhen, Wiley Online Library.wiley.com/doi/10.1002/tenm.202302514 by University Town Of Shenzhen, Wiley Online Library.wiley.com/doi/10.1002/tenm.202302514 by University Town Of Sh

and-conditions) on Wiley Online Library for rules of use; OA articles are governed

by the applicable Creative Commons

Keywords

full-cell performance, interfacial stability, presodiation, sodium ion batteries

Received: August 2, 2023 Revised: September 25, 2023 Published online: October 17, 2023

- [1] S.-W. Kim, D.-H. Seo, X. Ma, G. Ceder, K. Kang, Adv. Energy Mater. 2012, 2, 710.
- [2] T. Khan, A. K. Garg, A. Gupta, A. K. Madan, P. K. Jain, J. Energy Storage 2023. 57. 106204.
- [3] W. Zuo, A. Innocenti, M. Zarrabeitia, D. Bresser, Y. Yang, S. Passerini, *Acc. Chem. Res.* **2023**, *56*, 284.
- [4] Q. Liu, Z. Hu, M. Chen, C. Zou, H. Jin, S. Wang, S.-L. Chou, Y. Liu, S.-X. Dou, Adv. Funct. Mater. 2020, 30, 1909530.
- [5] Q. Liu, Z. Hu, M. Chen, C. Zou, H. Jin, S. Wang, S.-L. Chou, S.-X. Dou, Small 2019, 15, 1805381.
- [6] M. I. Jamesh, A. S. Prakash, J. Power Sources 2018, 378, 268.
- [7] Y. Bin Niu, Y. X. Yin, Y. G. Guo, Small 2019, 15, 1900233.
- [8] Z. Song, K. Zou, X. Xiao, X. Deng, S. Li, H. Hou, X. Lou, G. Zou, X. Ji, Chem. Eur. J. 2021, 27, 16082.
- [9] F. Xie, Y. Lu, L. Chen, Y.-S. Hu, Chin. Phys. Lett. 2021, 38, 118401.
- [10] K. Zou, W. Deng, P. Cai, X. Deng, B. Wang, C. Liu, J. Li, H. Hou, G. Zou, X. Ji, Adv. Funct. Mater. 2021, 31, 2005581.
- [11] W. Liu, X. Chen, C. Zhang, H. Xu, X. Sun, Y. Zheng, Y. Yu, S. Li, Y. Huang, J. Li, ACS Appl. Mater. Interfaces 2019, 11, 23207.
- [12] I. Moeez, H.-G. Jung, H.-D. Lim, K. Y. Chung, ACS Appl. Mater. Interfaces 2019, 11, 41394.
- [13] H. Wang, Y. Xiao, C. Sun, C. Lai, X. Ai, RSC Adv. 2015, 5, 106519.
- [14] S. Liu, M. Bai, X. Tang, W. Wu, M. Zhang, H. Wang, W. Zhao, Y. Ma, Chem. Eng. J. 2021, 417, 128997.
- [15] B. Shen, R. Zhan, C. Dai, Y. Li, L. Hu, Y. Niu, J. Jiang, Q. Wang, M. Xu, J. Colloid Interface Sci. 2019, 553, 524.
- [16] X. Pan, A. Chojnacka, F. Béguin, Energy Storage Mater. 2021, 40, 22.
- [17] J. H. Jo, J. U. Choi, Y. J. Park, J. K. Ko, H. Yashiro, S.-T. Myung, Energy Storage Mater. 2020, 32, 281.
- [18] X. Liu, Y. Tan, W. Wang, P. Wei, Z. W. Seh, Y. Sun, ACS Appl. Mater. Interfaces 2021, 13, 27057.
- [19] J. Song, M. Wu, K. Fang, T. Tian, R. Wang, H. Tang, J. Colloid Interface Sci. 2023, 630, 443.
- [20] X. Liu, Y. Tan, T. Liu, W. Wang, C. Li, J. Lu, Y. Sun, Adv. Funct. Mater. 2019, 29, 1903795.
- [21] M. Liu, Z. Yang, Y. Shen, S. Guo, J. Zhang, X. Ai, H. Yang, J. Qian, J. Mater. Chem. A 2021, 9, 5639.
- [22] M. Liu, J. Zhang, S. Guo, B. Wang, Y. Shen, X. Ai, H. Yang, J. Qian, ACS Appl. Mater. Interfaces 2020, 12, 17620.
- [23] S. Chen, Z. Wang, M. Zhang, X. Shi, L. Wang, W. An, Z. Li, F. Pan, L. Yang, Carbon Energy 2023, 5, e323.

- [24] S. Chen, Z. Wang, L. Wang, Z. Song, K. Yang, W. Zhao, L. Liu, J. Fang, G. Qian, F. Pan, L. Yang, Adv. Energy Sustain. Res. 2022, 3, 2200083.
- [25] G. Zheng, Q. Lin, J. Ma, J. Zhang, Y.-B. He, X. Tang, F. Kang, W. Lv, Q.-H. Yang, *InfoMat* 2021, 3, 1445.
- [26] F. Li, X. Yu, K. Tang, X. Peng, Q. Zhao, B. Li, J. Appl. Electrochem. 2022, 53. 9.
- [27] K. Fang, Y. Tang, J. Liu, Z. Sun, X. Wang, L. Chen, X. Wu, Q. Zhang, L. Zhang, Y. Qiao, S.-G. Sun, *Nano Lett.* 2023, 23, 6681.
- [28] Y. Shen, X. Shen, M. Yang, J. Qian, Y. Cao, H. Yang, Y. Luo, X. Ai, Adv. Funct. Mater. 2021, 31, 2101181.
- [29] J. Jang, I. Kang, J. Choi, H. Jeong, K.-W. Yi, J. Hong, M. Lee, Angew. Chem., Int. Ed. Engl. 2020, 59, 14473.
- [30] J. Choi, H. Jeong, J. Jang, A.-R. Jeon, I. Kang, M. Kwon, J. Hong, M. Lee, J. Am. Chem. Soc. 2021, 143, 9169.
- [31] S. Manzetti, T. Lu, J. Phys. Org. Chem. 2013, 26, 473.
- [32] T. Lu, S. Manzetti, Struct. Chem. 2014, 25, 1521.
- [33] B. Xiao, T. Rojo, X. Li, Chem Sus Chem 2019, 12, 133.
- [34] M. Song, Z. Yi, R. Xu, J. Chen, J. Cheng, Z. Wang, Q. Liu, Q. Guo, L. Xie, C. Chen, Energy Storage Mater. 2022, 51, 620.
- [35] J. A. S. Oh, G. Deysher, P. Ridley, Y.-T. Chen, D. Cheng, A. Cronk, S.-Y. Ham, D. H. S. Tan, J. Jang, L. H. B. Nguyen, Y. S. Meng, Adv. Energy Mater. 2023, 13, 2300776.
- [36] L. Xiao, H. Lu, Y. Fang, M. L. Sushko, Y. Cao, X. Ai, H. Yang, J. Liu, Adv. Energy Mater. 2018, 8, 1703238.
- [37] J. Chen, X. Fan, Q. Li, H. Yang, M. R. Khoshi, Y. Xu, S. Hwang, L. Chen, X. Ji, C. Yang, H. He, C. Wang, E. Garfunkel, D. Su, O. Borodin, C. Wang, Nat. Energy 2020, 5, 386.
- [38] H. Yildirim, A. Kinaci, M. K. Y. Chan, J. P. Greeley, ACS Appl. Mater. Interfaces 2015, 7, 18985.
- [39] L. Ji, M. Gu, Y. Shao, X. Li, M. H. Engelhard, B. W. Arey, W. Wang, Z. Nie, J. Xiao, C. Wang, J.-G. Zhang, J. Liu, Adv. Mater. 2014, 26, 2901.
- [40] Y. Ji, Z.-W. Yin, Z. Yang, Y.-P. Deng, H. Chen, C. Lin, L. Yang, K. Yang, M. Zhang, Q. Xiao, J.-T. Li, Z. Chen, S.-G. Sun, F. Pan, Chem. Soc. Rev. 2021. 50. 10743.
- [41] Y. Jin, P. M. L. Le, P. Gao, Y. Xu, B. Xiao, M. H. Engelhard, X. Cao, T. D. Vo, J. Hu, L. Zhong, B. E. Matthews, R. Yi, C. Wang, X. Li, J. Liu, J.-G. Zhang, Nat. Energy 2022, 7, 718.
- [42] L. A. Ma, A. J. Naylor, L. Nyholm, R. Younesi, Angew. Chem., Int. Ed. Engl. 2021, 60, 4855.
- [43] B. H. Toby, R. B. Von Dreele, J. Appl. Crystallogr 2013, 46, 544.
- [44] R. Baddour-Hadjean, J.-P. Pereira-Ramos, *Chem. Rev.* **2010**, *110*, 1278.
- [45] J. Zhang, F. Cheng, S. Chou, J. Wang, L. Gu, H. Wang, H. Yoshikawa, Y. Lu, J. Chen, Adv. Mater. 2019, 31, 1901808.
- [46] J. Xu, J. Zhang, T. P. Pollard, Q. Li, S. Tan, S. Hou, H. Wan, F. Chen, H. He, E. Hu, K. Xu, X.-Q. Yang, O. Borodin, C. Wang, *Nature* 2023, 614, 694.
- [47] H. Ji, J. Zhai, G. Chen, X. Qiu, H. Fang, T. Zhang, Z. Huang, W. Zhao, Z. Wang, M. Chu, R. Wang, C. Wang, R. Li, W. Zeng, X. Wang, Y. Xiao, Adv. Funct. Mater. 2022, 32, 2109319.
- [48] R. Jung, F. Linsenmann, R. Thomas, J. Wandt, S. Solchenbach, F. Maglia, C. Stinner, M. Tromp, H. A. Gasteiger, J. Electrochem. Soc. 2019, 166, A378.